Photoinduced processes in dye-sensitized photoanodes under the spotlight: a multiscale in silico investigation

Menzel, J.P.

CHAPTER 3

Understanding Coherent Charge Transfer: Isotope Effect and Dynamic Symmetry Breaking

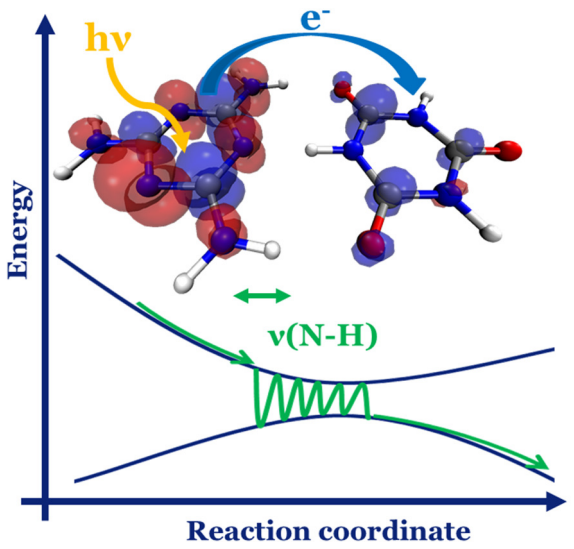

This Chapter is based on:

Jan Paul Menzel, Huub J.M. de Groot, Francesco Buda; *Journal of Physical Chemistry Letters*, **2019**, *10*, 6504-6511

3

ABSTRACT

Electron-nuclear (vibronic) coupling has emerged as an important factor in determining the efficiency of energy transfer and charge separation in natural and artificial photosynthetic systems. Here we investigate the photoinduced charge transfer process in a hydrogen bonded donor-acceptor molecular complex. By using real-time quantum-classical simulations based on time dependent Kohn-Sham we follow in detail the relaxation from the Franck-Condon point to the region of strong nonadiabatic coupling where electron transfer occurs. We elucidate how the charge transfer is coupled to specific vibrational modes and how it is affected by isotope substitution. The importance of resonance in nuclear and electron dynamics as well as the role of dynamic symmetry breaking is emphasized. Using the dipole moment as a descriptive parameter, exchange of angular momentum between nuclear and electronic subsystems in an electron-nuclear resonant process is inferred. The performed simulations support a nonadiabatic conversion via adiabatic passage process that was recently put forward. These results are relevant in deriving rational design principles for solar to fuel conversion devices.

3.1 Introduction

Photoinduced charge separation is a key process in photosynthesis. In nature, extended antenna complexes collect solar energy in the form of electronic excitations, which are then transferred to a reaction center, where the actual charge separation takes place.[1–3] Only after this separation, the photoenergy can be converted into chemical energy. Since ultrafast charge separation in combination with spatial separation play a major role in preventing charge recombination, understanding the origin of these fast and efficient processes is of crucial importance for the design of artificial photosynthesis devices.[4–8] Coherent charge transfer is an emerging concept, where, through vibronic coupling, nuclear vibrations resonate with specific electronic transitions, thus driving charge transfer efficiently.[9–14] Experimental observations and theoretical investigations underline the role of this effect in natural [12,15–21] as well as artificial systems.[22–27] For example, Falke *et al.* identified the C=C stretch and a pentagonal pinch mode to drive charge transfer from a polymer towards a fullerene in a polymer blend.[25]

Yet, essential aspects of coherent charge transfer are not well understood. In this work, using quantum-classical nonadiabatic Ehrenfest dynamics simulations, we explore which and how specific nuclear modes are selected in a donor-acceptor molecular complex and what role isotope effects and dynamic symmetry breaking play. Computer simulations of these processes provide the possibility of freezing specific nuclear coordinates or bond distances to assess how crucial these degrees of freedom are for the charge transfer. These exercises, though unphysical, can provide insight hardly accessible through experimental investigations. For this *in silico* investigation, we consider a DNA base pair mimic consisting of melamine and isocyanuric acid[22], which self-assemble through an extended two dimensional hydrogen bonding network[28]. This explicit donor-acceptor molecular complex combines relative simplicity with a realistic distribution of different chemical entities common in biological systems.[29] We investigate photoinduced coherent charge transfer and follow the onset of electron transfer (ET) upon photoexcitation in real

time. Through a comparison of the Fourier analysis of the nuclear and electronic motion along the same trajectory, relevant frequencies can be extracted. We find that modulating the frequency of key vibrational modes by isotope substitution changes their participation in the coherent process and increases the importance of other modes. Additionally, our investigations stress the importance of dynamic symmetry breaking for coherent charge transfer. Analogies are found between the simulation results of the photoinduced coherent charge transfer and the well-established adiabatic passage processes observed during nuclear magnetic resonance (NMR) adiabatic pulse[30] and chirped laser pulse optical spectroscopy experiments[31], providing additional support for the nonadiabatic conversion via adiabatic passage (NCAP)[9,32,33]. These results provide important principles to consider while designing and optimizing charge transfer and charge separation devices.[12,33]

3.2 Computational Methods

The structure of the DNA base pair mimic (melamine and isocyanuric acid) is given in scheme 3.1a. Geometry optimizations were performed with the Amsterdam Density Functional program[34,35] using Density Functional Theory (DFT). The BLYP exchange correlation functional[36,37] was used in combination with a Slater type basis set of the triple zeta with one polarization function (TZP)[38] quality. Dispersion corrections have been included following the formalism proposed by Grimme (DFT-D3)[39]. The electron transfer rate is distance dependent (see figure 3A.1 in the appendix), and we fix the nuclear coordinates of the nitrogen in the melamine tail as well as the oxygen in the isocyanuric tail that is furthest from the hydrogen bond interface. This avoids translational motion of the complex and maintains the relative distance, thereby mimicking the environment in a crystal or DNA backbone. Scheme 3.1b shows the relevant molecular orbitals involved in the photoinduced ET process. Upon excitation, an electron is transferred from the melamine HOMO to its LUMO (the LUMO+2 of the total complex, see scheme 3.1b).

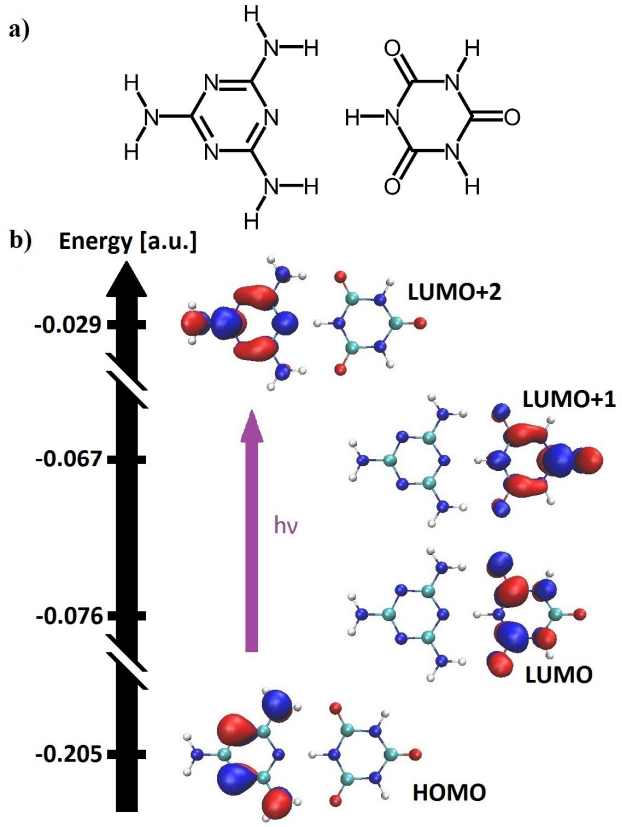

Scheme 3.1. a) Chemical structure of the pseudo base pair melamine (left, donor) and isocyanuric acid (right, acceptor) and **b)** Kohn-Sham orbitals relevant for the photoinduced charge transfer. The melamine is excited from its HOMO (HOMO of the total system) to its LUMO (the LUMO+2 of the total system), with the LUMO and LUMO+1 localized on the acceptor.

This excitation localized on the donor is higher in energy than the charge transfer state from HOMO to LUMO and from HOMO to LUMO+1. This is confirmed by TDDFT (both with BLYP and CAM-B3LYP) calculations, which show that the most relevant excitonic excitation on the donor has the highest oscillator strength in the energy range explored, while the charge transfer state has a lower energy[22] (see appendix 3A.2). This results in an energy gradient upon excitation from the excitonic to the charge transfer state. Ehrenfest dynamics simulations with BLYP[36,37] as exchange correlation functional are performed using the octopus program[40–43]. A nucleus centered spherical grid with a maximum radius of 7.56 Bohr for real space discretization was used; tests have been performed to find the optimal spacing (0.375 Bohr), resulting in a 70.18 Rydberg cut-off. Troullier-Martins pseudopotentials[44]

were used to describe the core electrons. The initial photoinduced electron configuration for the Ehrenfest dynamics was generated by moving one electron from the highest occupied β-orbital to the virtual β-LUMO+2: the β-HOMO occupation was changed to 0, while the β-LUMO+2 occupation was adapted to 1, representing a local excitation on the melamine as shown in scheme 3.1b. A time step of 1 attosecond is used for a total simulation length of 100 fs. The initial nuclear velocities are set to zero. Upon instantaneous excitation in the Franck-Condon region, the system starts to relax towards a more preferable geometry.

To quantify the electron transfer along the trajectory, we integrate the excess β-spin density localized on the acceptor. Since one β-electron is moved from the HOMO to the LUMO+2, β-spin density represents the density of the excited electron, while a lack of β-spin can be associated with the hole. This difference spin density was integrated over two halves of the simulation box, each containing the donor or acceptor molecule, respectively. The integrated density on the acceptor was then used to quantify the amount of electron density transferred during the Ehrenfest trajectory. A Fourier analysis of this electron transfer process was also done, using a gaussian window function with a sigma value of 0.8 to reduce noise.

3.3 Results and Discussion

Photoinduced Electron Transfer and Vibronic Coupling

The integrated (excited) electron density on the acceptor is reported over the trajectory from 0 to 100 fs in figure 3.1a. An oscillating character of the ET process, starting at about 10 fs, is clearly visible. The inset (top of figure 3.1) shows the difference spin density at the beginning and end of the simulation; at the beginning, HOMO and LUMO+2 can clearly be seen in the respective hole and electron densities.

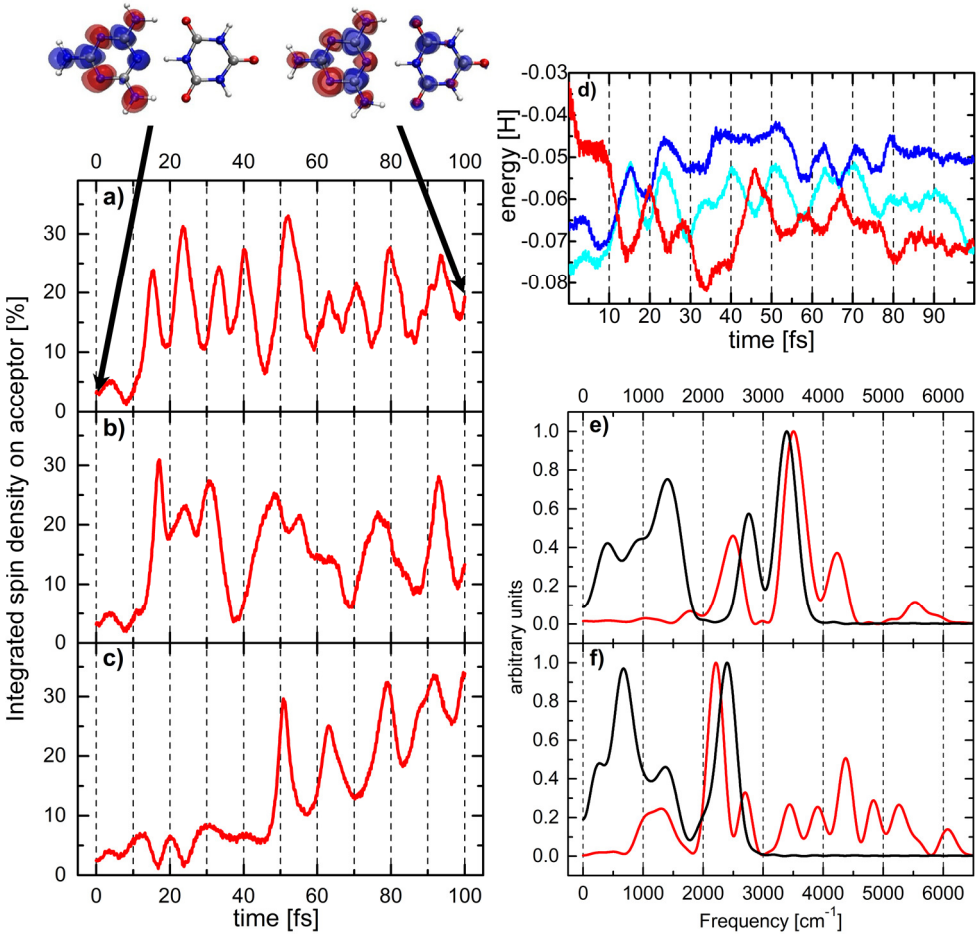

Figure 3.1. a) Electron transfer from the melamine (donor) to the isocyanuric acid (acceptor) quantified by β-spin density localized on the acceptor. Shown on top are snapshots of the difference between α and β spin density ($\rho(\beta) - \rho(\alpha)$) at the beginning and end of the simulation: blue shows excess β-spin density, corresponding to the excited electron, while red is the lack of β-spin density, which can be associated with the hole density. **b)** Electron transfer in fully deuterated melamine-isocyanuric acid system. **c)** Electron transfer for fully symmetrical starting geometry. **d)** Time evolution of the orbital energies of the LUMO+2 (red), LUMO+1 (dark blue) and LUMO (light blue) during the Ehrenfest dynamics simulation of panel a. **e)** Frequency spectrum associated to the electron transfer (red line) obtained by Fourier Transformation (FT) of the electron transfer time evolution shown in panel a and the total vibrational density of states (VDOS) of the pseudo base pair (black line) extracted from the corresponding nuclear trajectory. **f)** Electron transfer frequencies (red line) and total nuclear VDOS (black line) for the fully deuterated system corresponding to panel b.

At the end of the simulation, electron density has been transferred to the acceptor molecule partially populating the LUMO+1 and LUMO. The time evolution of the orbital energies in comparison to the electron transfer is shown in figure 3.1d).

After initial photoexcitation into the LUMO+2, a quick relaxation away from the Franck-Condon region takes place, bringing the orbital energy of the LUMO+2 closer to the LUMO and LUMO+1 energy levels in response to the nuclear motion. The orbital energies start rapidly approaching each other, crossing at approximately 12 fs, close to the first electron transfer maximum (see figure 3.1a). After the first crossing the orbital energies keep oscillating and crossing over time. However, we should keep in mind that this long-term behavior might be due to the mean field approach used, preventing the system to collapse to the lower potential energy surface. This is also the most likely reason why we do not observe complete conversion into the charge transfer state.

Noticeably, if the nuclear coordinates are fixed in the initial optimized geometry, no electron transfer is observed showing the crucial role of nuclear dynamics (see figure 3A.2 in section 3A.3 in the appendix). The Fourier transformation (FT) of the electron transfer time evolution can provide information on the characteristic frequencies associated to this process. Similarly, the total vibrational density of states (VDOS) can be extracted from the nuclear trajectory by performing a FT of the velocity autocorrelation function. In figure 3.1e, ET frequencies and the VDOS computed on the same trajectory corresponding to figure 3.1a are compared. In the frequency spectrum of the ET process, four major peaks can be distinguished at 2495, 3505, 4230 and 5525 cm^{-1} respectively. The two higher frequency peaks can be associated with electronic coherences. In particular, the peak at $\approx$ 4300 cm^{-1} can be assigned to electronic resonances close to the Franck-Condon point since it is prevalent in a purely electronic dynamics trajectory with fixed nuclear positions at the initial geometry (see figure 3A.3 in the appendix). A striking overlap between the VDOS and ET frequencies appears around 3500 cm^{-1}, corresponding to an oscillation time of 9.5 fs, suggesting strong electron-nuclear coupling. This peak in

the VDOS corresponds to the highest frequency modes, the N-H stretching vibrations (see figures 3A.4 to 3A.6 in the appendix, where peaks in the VDOS are assigned to specific nuclear motion). The lowest frequency peak in the ET spectrum at around 2500 cm^{-1} shows significant overlap with a peak in the VDOS associated to the central bridging N-H bond of the isocyanuric acid (see figure 3A.4). C=O stretches and other vibrational modes with $\nu < 2000\ cm^{-1}$ have a negligible effect on the ET frequency spectrum. Therefore, the N-H stretching modes appear to provide the important vibronic coupling, enabling charge transfer to take place.

Isotope Effect

If the N-H bond stretches are coupled to the photoinduced coherent charge transfer in this system, changing the corresponding vibrational frequency should affect the electron transfer process. Schnedermann *et al.* recently found that isotope effects play a significant role in the vibronically coherent process of photoisomerization of the 11-cis retinal[45]. To explore this hypothesis, we mimic *in silico* an isotope substitution experiment by exchanging all hydrogen atoms by the heavier deuterium isotope. Starting from otherwise identical initial conditions, we perform an Ehrenfest dynamics simulation for the fully deuterated system.

The isotope substitution results in a modified electron transfer pattern as shown in figure 3.1b. In particular, several oscillations at various frequencies contribute to the pattern. These frequencies are shown together with the total VDOS of the corresponding nuclear trajectory in figure 3.1f. The change in frequency of the N-D stretching modes compared to the N-H stretches is clearly visible and is proportional to about $\frac{1}{\sqrt{2}}$, as expected for a localized mode with substitution of ^{1}H by ^{2}D (see also figure 3A.7 in the appendix where a direct comparison of the VDOS for the deuterated and hydrogenated systems is shown). The two distinct N-H peaks (see figure 3.1e) merge in the N-D case, since the energy difference scales according to the isotope shift as well. The lower N-D peak appears as a shoulder at around 2000 cm^{-1}. The lower frequency bands involve C=O and C-N stretches as well as ring

modes and bending modes whose frequencies are not substantially affected by the isotope substitution.

In the high frequency region $\nu > 3000$ cm^{-1}, well resolved electronic frequencies are visible in the ET spectrum. The most dominant peak in the ET frequency spectrum $\nu \approx 2200$ cm^{-1} is resonant with the N-D stretching, as it is red shifted consistently with the shift in the N-D stretching frequency relative to the N-H mode. In addition to the N-D there is an overlap between the nuclear and electronic spectra in the lower frequency region $\nu \approx 1300$ cm^{-1} in contrast to the ^{1}H case. This indicates that also lower frequency nuclear vibrations, *e.g.* C=O and C-N stretching, couple with the ET process. These effects show that the resonance condition between the electronic energy difference and the nuclear vibrational frequencies changes upon isotope substitution. From this result we can already conclude that the N-H stretching is not uniquely essential for facilitating the electron transfer. What is important, is that these N-H modes - due to their high frequencies - are the first nuclear vibrations to match the energy difference between the electronic states during the relaxation process. The isotope substitution moves the resonance condition to lower frequencies. This is shown in a schematic potential energy plot along a generic nuclear relaxation coordinate (scheme 3.2). In the ^{2}D case additional nuclear modes couple to the electronic motion in contrast to the ^{1}H case, where the N-H frequencies are energetically isolated from all other modes.

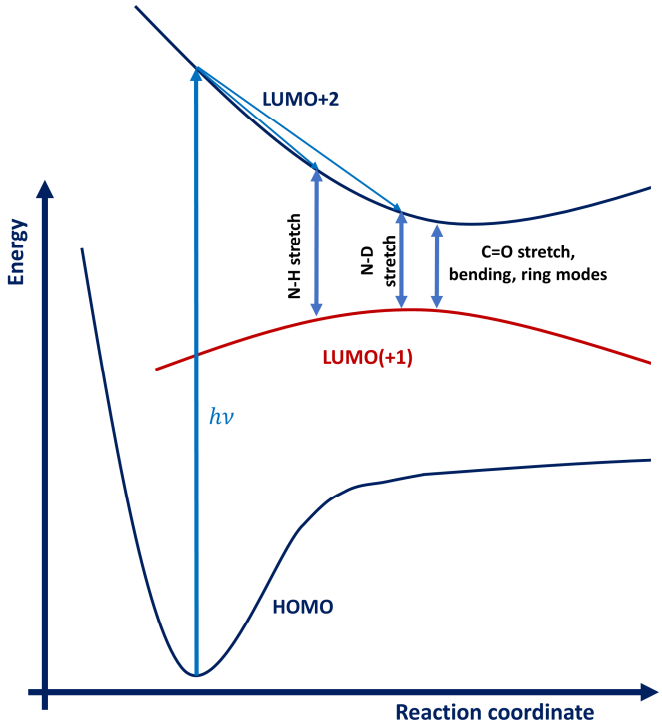

Scheme 3.2. Schematic representation of the coherent process in the investigated system. Upon excitation the system relaxes from the Franck Condon point (FC). In the ^{1}H system, the first available high energy vibrations are due to the N-H stretching and are well separated from the other modes. In the deuterated case, the N-D stretching has a vibrational energy similar to several other modes, which can therefore also couple to the electronic motion.

Dynamic Symmetry Breaking

To investigate the effect of symmetry on the photoinduced charge separation process, an Ehrenfest dynamics simulation was performed starting from an optimized geometry with enforced C_{2v} symmetry. The electron transfer pattern during this simulation can be seen in figure 3.1c, showing a delay of the first significant peak compared to the other two simulations (figure 3.1a, 3.1b). This is surprising considering that the orbital energy differences are small enough for resonant coupling with available nuclear modes within the first 10 fs (see figure 3A.8 in the appendix).

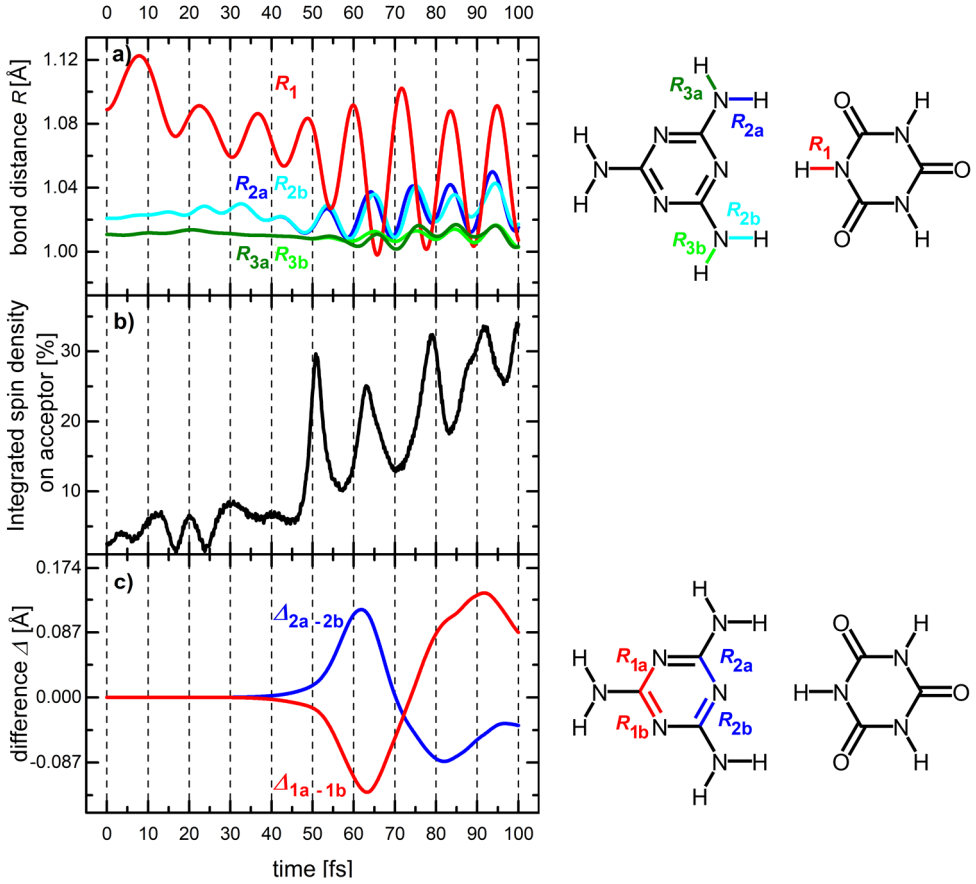

Figure 3.2. a) Time evolution of the N-H bond distances *R* for the donor-acceptor system with enforced starting C_{2v} symmetry. Different colors correspond to different bonds indicated in the chemical structure on the right. **b)** Electron transfer pattern for the same trajectory. **c)** Difference Δ in bond length *R* between symmetry equivalent C-N bonds shown in the chemical structure on the right.

To explain this suppression of coherent charge transfer, we need a more detailed investigation of the initial geometric relaxation. In figure 3.2a, the time evolution of the interfacial N-H bond distances (that were the most relevant in the previous cases) is compared with the electron transfer (figure 3.2b).

Two main messages can be extracted from figure 3.2a: *i*) Upon electronic excitation, symmetry equivalent bonds with respect to the C_2-axis (2a and 2b; 3a and 3b) are evolving in a perfectly identical manner, maintaining the C_{2v}-symmetry. Only when the electron transfer starts, the deviation from C_{2v}-symmetry gradually

increases from around 50 fs. *ii*) The amplitude of the N-H bond oscillations increases dramatically during the electron transfer process, suggesting that electronic energy is transferred into these nuclear vibrations.

The question arises whether the electron transfer induces this divergence from the C_{2v} symmetric motion, or conversely, it is the breaking of symmetry that allows for the electron transfer in the first place. To address this question, it is helpful to look at the difference in bond length between symmetry equivalent bonds with respect to the C_2-axis. We find that the pairs of bonds that first diverge from perfect symmetric motion are C-N bonds in the aromatic ring of the donor molecule (see figure 3A.9 in the appendix showing all symmetry equivalent pairs). In figure 3.2c, the bond length difference $\Delta_{1a-1b} = R_{1a} - R_{1b}$ between the two bonds 1a and 1b, as well as the bond length difference $\Delta_{2a-2b} = R_{2a} - R_{2b}$ between bonds 2a and 2b are shown. At $t \approx$ 35 fs, the bond lengths start to diverge: bond 1a shortens, while 1b elongates and at the same time bond 2a increases while bond 2b decreases in length. The combination of these concerted expansions and compressions corresponds to a normal mode of the donor molecule of the A_2' irreducible representation of the D3h group which is the point group of both melamine and isocyanuric acid when in isolation. This A_2' irreducible representation also includes rotation around the z axis which is oriented perpendicular to the molecular plane. This motion breaks the initial C_{2v}-symmetry. Two equivalent modes rotating in opposite directions around the z-axis exist that could be excited. Once a small preference, for instance due to numerical noise in the integration of the equations of motion, is given to a rotation in one direction in favor of its counter rotating equivalent, asymmetric motion will emerge. About 45 fs into the simulation, which is around 10 fs after the onset of the asymmetric motion, the electron transfer process starts, responding to the breaking of symmetry. This underlines the importance of dynamic symmetry breaking in photoinduced coherent charge transfer. In a system interacting with its environment, there will always be a slight preference to one component over the other, resulting in symmetry breaking. This holds especially true when coupled to a thermal bath or in a chiral environment.

The displacement from the symmetric geometry, at t = 45 fs, when the ET process starts, is about 0.01 Å. This small displacement will already be present at extremely low temperatures. Still, these results already suggest a design principle for systems to optimize coherent charge transfer: breaking the symmetry as initial condition, *e.g.* by using chiral motifs. This principle is well in line with natural photosynthetic systems, which are built from chiral proteins and cofactors.[46,47]

Similarities with other Adiabatic Passage Processes

We stress the similarity between the coherent charge transfer and the well-established adiabatic passage processes observed during adiabatic pulses in both NMR and optical spectroscopy[30,31]: In this work we have a process that can be described as population change between two states - an excitonic and a charge transfer state. The two states have an energy difference corresponding to a radial frequency ω_e, that is modulated over time due to relaxation from the Franck Condon point (see scheme 3.2). This closely mirrors the radiofrequency ω_{rf} in an NMR adiabatic pulse experiment and the laser frequency ω_L in a chirped laser pulse in optical spectroscopy. In all three cases, we sweep towards a resonance condition, in our case $\omega_e = \omega_n$, with ω_n being an available nuclear frequency. As we approach the resonance, nonadiabatic coupling increases significantly. The electronic motion slows down, the time scales of nuclear and electronic motion converge, making exchange between the nuclear and electronic system possible by vibronic coupling. As in the two adiabatic passage processes mentioned earlier, (*i*) the NMR adiabatic pulse for reversal of magnetization, and (*ii*) chirped laser pulses with change of orbital angular momentum, a change of population from the excitonic state to the charge transfer state can be observed (see electron transfer in figure 3.1a-c), showing characteristic oscillations of frequency ω_n. Moving into the interaction frame corresponding to this ω_n, this exchange should then be smooth, again similar to the mentioned other processes. Within the interaction frame of the electronic frequency ω_e however, similarly to the case of the interaction frame of the laser pulse in optical

spectroscopy or the radio frequency in an adiabatic pulse experiment in NMR, there is a precession around the interaction frame axis, due to the mismatch of ω_e and ω_n when sweeping ω_e. At the resonance condition $\omega_e = \omega_n$, the nonadiabatic coupling is strongest and the populations of state 1 and 2 will be $p_1 = p_2 = ½$ each. As the system moves out of resonance, with $\omega_e < \omega_n$, the system further evolves into full conversion with $p_1 = 0$ and $p_2 = 1$. In our simulation, due to the mean field approach used, we cannot observe this full conversion, since the system is trapped in the coherent superposition state and does not collapse into an adiabatic state (see chapter 2.5). Still, due to the many parallels observed between this coherent charge transfer process on one side and adiabatic pulses and chirped laser pulse experiments on the other side, our results support a nonadiabatic conversion via adiabatic passage (NCAP) process.

Exchange of Angular Momentum

Since the system evolves from one quantum state to another, a change of quantum number is involved. Normally, transitions between electronic states follow selection rules, leading to transitions only being allowed via *e.g.* the release or absorption of a photon carrying an angular momentum. Also for the non-radiative exciton to charge transfer transition in our study the change in quantum number has to be accompanied by a change of an associated physical quantity. In a publication by Purchase *et al.*, the authors stressed the importance of convergence of time scales of nuclear and electronic circulating motion in a molecule for coherent charge transfer and suggested the exchange of angular momentum between the electronic and nuclear subsystems in a semiclassical coherent process.[32] Coupling of quantum and classical rotation is well established in other fields of chemistry and chemical physics, where it has been shown that transitions in quantum subspaces give rise to observable rotations in a suitable interaction frame of the classical motion.[48] Since in the Ehrenfest simulations, the conservation of total angular momentum is not enforced, we rather monitor collective motion in both the electronic as well as nuclear

subsystems by following the orientational change in the electronic and nuclear components of the dipole moment, which we introduce here as a descriptive parameter for the process. The generated charge transfer state results in a large electronic dipole moment change along the *x*-axis, potentially masking any other orientational change. Therefore, we focus on the dipole moment associated with the α-electrons since they are not directly involved in the charge transfer process and yet still respond to the electron transfer. The orientation of this dipole moment in the *x*-*y* plane during the Ehrenfest dynamics with symmetric starting condition is shown in figure 3.3a.

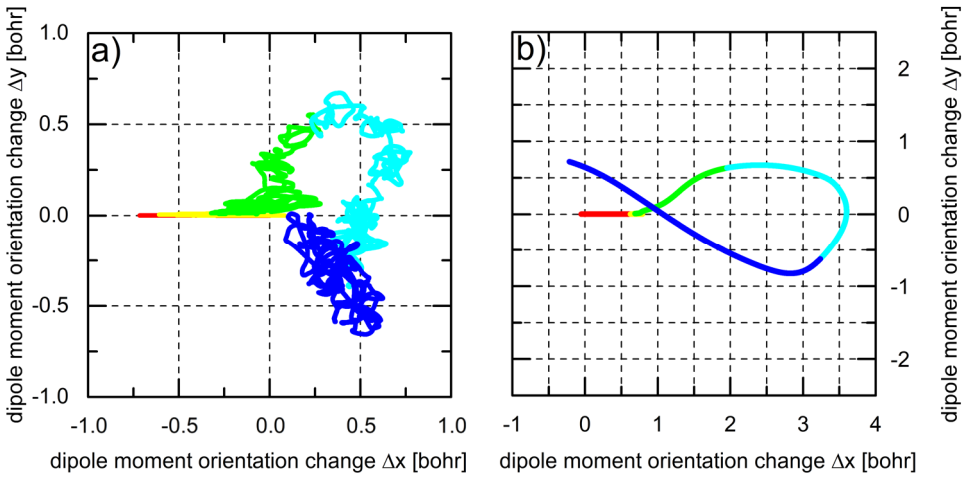

Figure 3.3. a) Orientation of the dipole moment associated with *α*-electrons in the *x*-*y* plane for the simulation starting with enforced symmetric geometry. The colors correspond to consecutive time intervals, starting from red (0<*t*<20 fs) to yellow (20<*t*<40 fs), green (40<*t*<60 fs), light blue (60<*t*<80 fs) and dark blue (80<*t*<100 fs). The rotational character starting around *t* = 40 fs is clearly visible. **b)** Change of orientation of the dipole moment associated with the nitrogen and hydrogen nuclei involved in the N-H stretches coupled to the electron transfer process. The colors correspond to consecutive time intervals, starting from red (0<*t*<20 fs) to yellow (20<*t*<40 fs), green (40<*t*<60 fs), light blue (60<*t*<80 fs) and dark blue (80<*t*<100 fs). The correlation between this nuclear dipole moment orientation and the electronic dipole moment orientation in a) is apparent.

Within the first ~35 fs, the dipole moment only changes along the *x*-axis, conserving symmetry. Upon the breaking of symmetry, the dipole moment starts to deviate from its initial orientation along the *x*-axis. At around *t* = 45 fs, when the

electron transfer process starts, a clear clockwise rotation with an angular momentum in the negative *z*-axis direction starts.

According to Purchase *et al.*, this change in electronic angular momentum should be associated with a net rotation in the interaction frame of the nuclear motion of the coupled mode.[32] We should therefore see the same rotational behavior if we plot the dipole moment orientation change of all the nuclei involved in N-H covalent bond vibrations, which we have shown to be crucial for the coherent photoinduced charge transfer. The change in this nuclear dipole moment orientation reflects the net rotation in the interaction frame associated with the nuclear mode and is shown in figure 3.3b. There is a clear correlation in the rotation of this nuclear dipole moment and the rotation of the dipole moment associated with the α-electrons. After about 35 fs, the symmetry breaks, leading to deviation of both dipole moment orientations from the *x*-axis. At around $t = 45$ fs, at the onset of electron transfer, both the nuclear as well as electronic dipole moment start to rotate in unison in the molecular plane, maintaining correlation until about 80 fs into the simulation, where noise in the electronic system appears to obscure this connection. The change in quantum number therefore involves the gradual exchange of angular momentum between the electronic and nuclear system. For completeness, the dipole moment associated with the β-spin density in the symmetric case and the dipole moment associated with the α-electrons in the asymmetric simulation shown in figures 3A.10 and 3A.11 in the appendix.

3.4 Conclusion

In summary, the photoinduced coherent charge transfer in this donor-acceptor system can be described as follows: Upon excitation into the Franck-Condon region in the excited state localized on the donor molecule, the system relaxes towards lower energetic regions of the excited state PES. During this relaxation, the system explores regions of strong coupling between the excitonic and lower energy charge transfer states as they approach each other energetically. As soon as the energy difference between these two states (one occupied, one unoccupied), is in resonance with a nuclear vibration available in the system, the nuclear vibration couples to the electronic motion and drives the electron transfer in a resonant process. A crucial condition for an efficient conversion process is the dynamic breaking of symmetry. Furthermore, the change in quantum number associated with the non-radiative transition between quantum states leads to a net exchange of angular momentum into the coupled vibrational state. Which particular nuclear mode first reaches the resonance condition depends on the specific potential energy surfaces involved in the electron transfer process. Thus, the process is robust as it self-selects a rapid channel to the output. In the melamine-isocyanuric acid system the highest N-H bond frequencies are the first and most important modes reaching the resonance condition. Due to the energetic gap between the N-H stretches and all other modes, the N-H bonds drive the electron transfer almost exclusively. This results in a relatively clean oscillatory pattern in the electron transfer process. When exchanging hydrogens by deuterium, the system relaxes to a region where the involved states are closer in energy. The difference between the N-D stretches and the lower frequency modes is now smaller and thus additional modes can drive the charge transfer. Therefore, more frequencies are involved and a more complex electron transfer pattern emerges. In spite of the specificity of this donor-acceptor complex, we believe these principles are playing a role in natural systems and might help interpreting experimental data on coherent charge transfer.

3.5 References

(1) Groot, M. L.; Pawlowicz, N. P.; Wilderen, L. J. G. W. van; Breton, J.; Stokkum, I. H. M. van; Grondelle, R. van. Initial Electron Donor and Acceptor in Isolated Photosystem II Reaction Centers Identified with Femtosecond Mid-IR Spectroscopy. *PNAS* **2005**, *102* (37), 13087–13092.

(2) Durrant, J. R.; Klug, D. R.; Kwa, S. L.; Grondelle, R. van; Porter, G.; Dekker, J. P. A Multimer Model for P680, the Primary Electron Donor of Photosystem II. *PNAS* **1995**, *92* (11), 4798–4802.

(3) Romero, E.; van Stokkum, I. H. M.; Novoderezhkin, V. I.; Dekker, J. P.; van Grondelle, R. Two Different Charge Separation Pathways in Photosystem II. *Biochemistry* **2010**, *49* (20), 4300–4307.

(4) Faunce, T. A.; Lubitz, W.; Rutherford, A. W. (Bill); MacFarlane, D.; Moore, G. F.; Yang, P.; Nocera, D. G.; Moore, T. A.; Gregory, D. H.; Fukuzumi, S.; Yoon, K. B.; Armstrong, F. A.; Wasielewski, M. R.; Styring, S. Energy and Environment Policy Case for a Global Project on Artificial Photosynthesis. *Energy Environ. Sci.* **2013**, *6* (3), 695–698.

(5) Faunce, T.; Styring, S.; Wasielewski, M. R.; Brudvig, G. W.; Rutherford, A. W.; Messinger, J.; Lee, A. F.; Hill, C. L.; deGroot, H.; Fontecave, M.; MacFarlane, D. R.; Hankamer, B.; Nocera, D. G.; Tiede, D. M.; Dau, H.; Hillier, W.; Wang, L.; Amal, R. Artificial Photosynthesis as a Frontier Technology for Energy Sustainability. *Energy Environ. Sci.* **2013**, *6* (4), 1074–1076.

(6) Tachibana, Y.; Vayssieres, L.; Durrant, J. R. Artificial Photosynthesis for Solar Water-Splitting. *Nat Photon* **2012**, *6* (8), 511–518.

(7) Kim, D.; Sakimoto, K. K.; Hong, D.; Yang, P. Artificial Photosynthesis for Sustainable Fuel and Chemical Production. *Angew. Chem. Int. Ed.* **2015**, *54* (11), 3259–3266.

(8) Yu, Z.; Li, F.; Sun, L. Recent Advances in Dye-Sensitized Photoelectrochemical Cells for Solar Hydrogen Production Based on Molecular Components. *Energy Environ. Sci.* **2015**, *8* (3), 760–775.

(9) Scholes, G. D. Coherence from Light Harvesting to Chemistry. *J. Phys. Chem. Lett.* **2018**, *9* (7), 1568–1572.

(10) Jumper, C. C.; Rafiq, S.; Wang, S.; Scholes, G. D. From Coherent to Vibronic Light Harvesting in Photosynthesis. *Current Opinion in Chemical Biology* **2018**, *47*, 39–46.

(11) Scholes, G. D.; Fleming, G. R.; Olaya-Castro, A.; van Grondelle, R. Lessons from Nature about Solar Light Harvesting. *Nat Chem* **2011**, *3* (10), 763–774.

(12) Romero, E.; Augulis, R.; Novoderezhkin, V. I.; Ferretti, M.; Thieme, J.; Zigmantas, D.; van Grondelle, R. Quantum Coherence in Photosynthesis for Efficient Solar-Energy Conversion. *Nat Phys* **2014**, *10* (9), 676–682.

(13) Scholes, G. D.; Fleming, G. R.; Chen, L. X.; Aspuru-Guzik, A.; Buchleitner, A.; Coker, D. F.; Engel, G. S.; van Grondelle, R.; Ishizaki, A.; Jonas, D. M.; Lundeen, J. S.; McCusker, J. K.; Mukamel, S.; Ogilvie, J. P.; Olaya-Castro, A.; Ratner, M. A.; Spano, F. C.; Whaley, K. B.; Zhu, X. Using Coherence to Enhance Function in Chemical and Biophysical Systems. *Nature* **2017**, *543* (7647), 647–656.

(14) Chenu, A.; Scholes, G. D. Coherence in Energy Transfer and Photosynthesis. *Annual Review of Physical Chemistry* **2015**, *66* (1), 69–96.

(15) Engel, G. S.; Calhoun, T. R.; Read, E. L.; Ahn, T.-K.; Mančal, T.; Cheng, Y.-C.; Blankenship, R. E.; Fleming, G. R. Evidence for Wavelike Energy Transfer through Quantum Coherence in Photosynthetic Systems. *Nature* **2007**, *446* (7137), 782–786.

(16) Fuller, F. D.; Pan, J.; Gelzinis, A.; Butkus, V.; Senlik, S. S.; Wilcox, D. E.; Yocum, C. F.; Valkunas, L.; Abramavicius, D.; Ogilvie, J. P. Vibronic Coherence in Oxygenic Photosynthesis. *Nature Chemistry* **2014**, *6* (8), 706–711.

(17) Collini, E.; Wong, C. Y.; Wilk, K. E.; Curmi, P. M. G.; Brumer, P.; Scholes, G. D. Coherently Wired Light-Harvesting in Photosynthetic Marine Algae at Ambient Temperature. *Nature* **2010**, *463* (7281), 644–647.

(18) Tiwari, V.; Peters, W. K.; Jonas, D. M. Electronic Resonance with Anticorrelated Pigment Vibrations Drives Photosynthetic Energy Transfer Outside the Adiabatic Framework. *PNAS* **2013**, *110* (4), 1203–1208.
(19) Thyrhaug, E.; Tempelaar, R.; Alcocer, M. J. P.; Žídek, K.; Bína, D.; Knoester, J.; Jansen, T. L. C.; Zigmantas, D. Identification and Characterization of Diverse Coherences in the Fenna–Matthews–Olson Complex. *Nature Chemistry* **2018**, *10* (7), 780–786.
(20) Ma, F.; Romero, E.; Jones, M. R.; Novoderezhkin, V. I.; van Grondelle, R. Vibronic Coherence in the Charge Separation Process of the Rhodobacter Sphaeroides Reaction Center. *J. Phys. Chem. Lett.* **2018**, *9* (8), 1827–1832.
(21) Chin, A. W.; Prior, J.; Rosenbach, R.; Caycedo-Soler, F.; Huelga, S. F.; Plenio, M. B. The Role of Non-Equilibrium Vibrational Structures in Electronic Coherence and Recoherence in Pigment-Protein Complexes. *Nat Phys* **2013**, *9* (2), 113–118.
(22) Eisenmayer, T. J.; Buda, F. Real-Time Simulations of Photoinduced Coherent Charge Transfer and Proton-Coupled Electron Transfer. *ChemPhysChem* **2014**, *15* (15), 3258–3263.
(23) Akimov, A. V.; Neukirch, A. J.; Prezhdo, O. V. Theoretical Insights into Photoinduced Charge Transfer and Catalysis at Oxide Interfaces. *Chem. Rev.* **2013**, *113* (6), 4496–4565.
(24) Monti, A.; Negre, C. F. A.; Batista, V. S.; Rego, L. G. C.; de Groot, H. J. M.; Buda, F. Crucial Role of Nuclear Dynamics for Electron Injection in a Dye–Semiconductor Complex. *J. Phys. Chem. Lett.* **2015**, *6* (12), 2393–2398.
(25) Falke, S. M.; Rozzi, C. A.; Brida, D.; Maiuri, M.; Amato, M.; Sommer, E.; Sio, A. D.; Rubio, A.; Cerullo, G.; Molinari, E.; Lienau, C. Coherent Ultrafast Charge Transfer in an Organic Photovoltaic Blend. *Science* **2014**, *344* (6187), 1001–1005.
(26) Andrea Rozzi, C.; Maria Falke, S.; Spallanzani, N.; Rubio, A.; Molinari, E.; Brida, D.; Maiuri, M.; Cerullo, G.; Schramm, H.; Christoffers, J.; Lienau, C. Quantum Coherence Controls the Charge Separation in a Prototypical Artificial Light-Harvesting System. *Nat Commun* **2013**, *4*, 1602.
(27) Park, M.; Im, D.; Rhee, Y. H.; Joo, T. Coherent and Homogeneous Intramolecular Charge-Transfer Dynamics of 1-Tert-Butyl-6-Cyano-1,2,3,4-Tetrahydroquinoline (NTC6), a Rigid Analogue of DMABN. *J. Phys. Chem. A* **2014**, *118* (28), 5125–5134.
(28) Perdigão, L. M. A.; Champness, N. R.; Beton, P. H. Surface Self-Assembly of the Cyanuric Acid–Melamine Hydrogen Bonded Network. *Chem. Commun.* **2006**, *0* (5), 538–540.
(29) Prokhorenko, V. I.; Picchiotti, A.; Pola, M.; Dijkstra, A. G.; Miller, R. J. D. New Insights into the Photophysics of DNA Nucleobases. *The Journal of Physical Chemistry Letters* **2016**, *7* (22), 4445–4450.
(30) Tannús, G. Adiabatic Pulses. *NMR IN BIOMEDICINE* **1997**, *10*, 12.
(31) Wollenhaupt, M.; Präkelt, A.; Sarpe-Tudoran, C.; Liese, D.; Baumert, T. Quantum Control by Selective Population of Dressed States Using Intense Chirped Femtosecond Laser Pulses. *Appl. Phys. B* **2006**, *82* (2), 183–188.
(32) Purchase R. L.; de Groot H. J. M. Biosolar Cells: Global Artificial Photosynthesis Needs Responsive Matrices with Quantum Coherent Kinetic Control for High Yield. *Interface Focus* **2015**, *5* (3), 20150014.
(33) Purchase, R.; Cogdell, R.; Breitling, F.; Stadler, V.; van Hulst, N.; Kramer, G.-J.; Ramirez, A.; Zwijnenberg, R.; Kallergi, A.; de Baan, J. B.; Rudra, I.; de Groot, H. J. M. Semi-Synthetic Responsive Matrices for Artificial Photosynthesis. In *Series on Chemistry, Energy and the Environment*; WORLD SCIENTIFIC, 2019; pp 47–69.
(34) Velde, G. te; Bickelhaupt, F. M.; Baerends, E. J.; Fonseca Guerra, C.; van Gisbergen, S. J. A.; Snijders, J. G.; Ziegler, T. Chemistry with ADF. *J. Comput. Chem.* **2001**, *22* (9), 931–967.
(35) ADF2013, http://www.scm.com, SCM, Theoretical Chemistry, Vrije Universiteit, Amsterdam, The Netherlands. .
(36) Becke, A. D. Density-Functional Exchange-Energy Approximation with Correct Asymptotic Behavior. *Phys. Rev. A* **1988**, *38* (6), 3098–3100.
(37) Lee, C.; Yang, W.; Parr, R. G. Development of the Colle-Salvetti Correlation-Energy Formula into a Functional of the Electron Density. *Phys. Rev. B* **1988**, *37* (2), 785–789.

(38) Van Lenthe, E.; Baerends, E. J. Optimized Slater-Type Basis Sets for the Elements 1–118. *Journal of Computational Chemistry* **2003**, *24*, 1142–1156.
(39) Grimme; others. A Consistent and Accurate Ab Initio Parametrization of Density Functional Dispersion Correction (DFT-D) for the 94 Elements H-Pu. *J. Chem. Phys.* **2010**, *132* (715).
(40) Andrade, X.; Alberdi-Rodriguez, J.; Strubbe, D. A.; Oliveira, M. J. T.; Fernando Nogueira; Castro, A.; Muguerza, J.; Arruabarrena, A.; Louie, S. G.; Aspuru-Guzik, A.; Angel Rubio; Marques, M. A. L. Time-Dependent Density-Functional Theory in Massively Parallel Computer Architectures: The Octopus Project. *J. Phys.: Condens. Matter* **2012**, *24* (23), 233202.
(41) Castro, A.; Appel, H.; Oliveira, M.; Rozzi, C. A.; Andrade, X.; Lorenzen, F.; Marques, M. a. L.; Gross, E. K. U.; Rubio, A. Octopus: A Tool for the Application of Time-Dependent Density Functional Theory. *physica status solidi (b)* **2006**, *243* (11), 2465–2488.
(42) Marques, M. A. L.; Castro, A.; Bertsch, G. F.; Rubio, A. Octopus: A First-Principles Tool for Excited Electron–Ion Dynamics. *Computer Physics Communications* **2003**, *151* (1), 60–78.
(43) Castro, A.; Marques, M. A. L.; Rubio, A. Propagators for the Time-Dependent Kohn–Sham Equations. *The Journal of Chemical Physics* **2004**, *121* (8), 3425–3433.
(44) Troullier, N.; Martins, J. L. Efficient Pseudopotentials for Plane-Wave Calculations. *Phys. Rev. B* **1991**, *43* (3), 1993–2006.
(45) Schnedermann, C.; Yang, X.; Liebel, M.; Spillane, K. M.; Lugtenburg, J.; Fernández, I.; Valentini, A.; Schapiro, I.; Olivucci, M.; Kukura, P.; Mathies, R. A. Evidence for a Vibrational Phase-Dependent Isotope Effect on the Photochemistry of Vision. *Nature Chem* **2018**, *10* (4), 449–455.
(46) Eisenmayer, T. J.; de Groot, H. J. M.; van de Wetering, E.; Neugebauer, J.; Buda, F. Mechanism and Reaction Coordinate of Directional Charge Separation in Bacterial Reaction Centers. *J. Phys. Chem. Lett.* **2012**, *3* (6), 694–697.
(47) Moore, L. J.; Zhou, H.; Boxer, S. G. Excited-State Electronic Asymmetry of the Special Pair in Photosynthetic Reaction Center Mutants: Absorption and Stark Spectroscopy. *Biochemistry* **1999**, *38* (37), 11949–11960.
(48) Boender, G. J.; Vega, S.; Groot, H. J. M. D. A Physical Interpretation of the Floquet Description of Magic Angle Spinning Nuclear Magnetic Resonance Spectroscopy. *Molecular Physics* **1998**, *95* (5), 921–934.

3.A Appendix

3A.1 Geometries and Effect of Intermolecular Distance

In figure 3A.1, we show the electron transfer time evolution for a trajectory with an intermolecular distance increased by 1 Å compared to the optimized geometry. As is clearly visible, this is already enough to inhibit the charge transfer process on the time scale of the simulation.

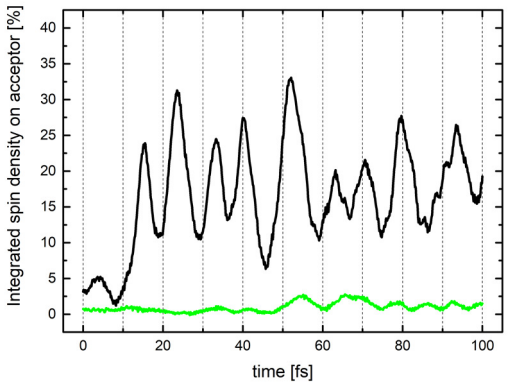

Figure 3A.1. Comparison of the electron transfer pattern starting from optimized geometry (black) and a geometry with an intermolecular distance increased by 1Å (green). This increase in intermolecular distance is enough to inhibit the charge transfer process within the time scale investigated.

The initial geometries used for the Ehrenfest dynamics are given in tables 3A.1

Table 3A.1. Initial geometry (in Bohr) used for the Ehrenfest dynamics a) without enforced C_{2v}-symmetry and b) with enforced C_{2v}-symmetry. The fixed atoms are marked with *

a)				**b)**			
N	-2.001614	0.031842	0.000000	N	-2.603536	0.000000	0.000000
C	-3.426373	-2.135237	0.000000	C	-3.999683	-2.168130	0.000000
C	-3.379525	2.278876	0.000000	C	-3.999683	2.168130	0.000000
N	-5.992697	-2.227231	0.000000	N	-6.546495	-2.279433	0.000000
N	-5.949866	2.399089	0.000000	N	-6.546495	2.279433	0.000000
C	-7.117530	0.115311	0.000000	C	-7.692047	0.000000	0.000000
N	-2.123401	4.418507	0.000000	N	-2.739492	4.396637	0.000000
N	-2.233755	-4.326562	0.000000	N	-2.739492	-4.396637	0.000000
N	-9.614457	0.117436	0.000000 *	N	-10.268718	0.000000	0.000000 *
H	-0.114494	4.450706	0.000000	H	-0.811858	4.473371	0.000000
H	-3.121367	6.044066	0.000000	H	-3.780779	5.997919	0.000000
H	-3.274394	-5.947841	0.000000	H	-3.780779	-5.997919	0.000000
H	-0.239847	-4.434270	0.000000	H	-0.811858	-4.473371	0.000000
H	-10.533707	1.851824	0.000000	H	-11.205478	1.663445	0.000000
H	-10.585442	-1.583609	0.000000	H	-11.205478	-1.663445	0.000000
C	8.517469	-0.165043	0.000000	C	7.978317	0.000000	0.000000
N	7.061556	-2.324476	0.000000	N	6.508749	-2.192863	0.000000
N	7.095488	2.110390	0.000000	N	6.508749	2.192863	0.000000
C	4.427971	-2.407892	0.000000	C	3.868282	-2.314315	0.000000
C	4.517363	2.253758	0.000000	C	3.868282	2.314315	0.000000
N	3.358169	-0.044253	0.000000	N	2.646694	0.000000	0.000000
O	10.757456	-0.132269	0.000000 *	O	10.286523	0.000000	0.000000 *
O	3.346296	4.294753	0.000000	O	2.763579	4.365135	0.000000
O	3.319715	-4.429777	0.000000	O	2.763579	-4.365135	0.000000
H	7.996239	-3.989308	0.000000	H	7.449109	-3.869490	0.000000
H	8.097476	3.783894	0.000000	H	7.449109	3.869490	0.000000
H	1.213266	-0.002685	0.000000	H	0.588848	0.000000	0.000000

3A.2 Excitation energies with Time dependent DFT

To classify important electronic excitations of the pseudo base pair system, linear-response time dependent DFT calculations were performed with the Amsterdam Density Functional program (ADF)[1,2]. Since BLYP[3,4] is known to poorly describe charge transfer excitations, we calculated the first 30 excitations using also the long range corrected CAM-B3LYP[5] exchange correlation functional and a TZP[6] basis set with D3 dispersion corrections[7]. The relative orbital alignment of the relevant orbitals for BLYP and CAM-B3LYP are given as energy differences in table 3A.2.

Table 3A.2. Orbital energy differences between HOMO/LUMO, LUMO/LUMO+1 and LUMO+1/LUMO+2 for BLYP and CAM-B3LYP.

Transition	BLYP	CAM-B3LYP
ΔE LUMO-HOMO [Hartree]	0.129	0.308
ΔE (LUMO+1)-LUMO [Hartree]	0.009	0.006
ΔE (LUMO+2)-(LUMO+1) [Hartree]	0.038	0.031

As expected for a hybrid functional, the HOMO-LUMO gap is significantly increased in CAM-B3LYP in comparison to the GGA BLYP. However, there is no rearrangement in the four relevant orbitals active in the charge transfer process. Excitation energies and oscillator strengths for the most relevant excitonic and charge transfer excitations are reported in table 3A.3. As expected for a GGA functional, BLYP strongly underestimates the charge transfer excitation energy. However, for both functionals, the energy of the excitonic state is higher in comparison to the charge transfer state. Furthermore, the oscillator strength of the excitonic state is in both cases larger than for the charge transfer state.

Table 3A.3. Excitation energies and Oscillator strength for the most relevant charge transfer and exciton excited states in the melamine-isocyanuric acid pseudo base pair determined by TDDFT with BLYP and CAM-B3LYP.

	BLYP		CAM-B3LYP	
	Energy [eV]	Oscillator strength	Energy [eV]	Oscillator strength
Charge transfer excitation	3.680	0.0037	6.407	0.1220
Excitonic excitation localized on the donor	6.1834	0.2767	6.905	0.6140

3A.3 Ehrenfest dynamics with frozen nuclear geometry

Electron dynamics simulations were performed with fixed nuclear degrees of freedom. Two different geometries were investigated: the initial geometry at the start of the Ehrenfest dynamics (from here on called simulation G0) and the geometry from the Ehrenfest trajectory at 10.7 fs, approximately the time where the electron transfer process starts (named simulation G1). The latter geometry lies therefore within the region where the involved electronic states are closely coupled. The total simulation time was 50 fs with a time step of 1 as. The integrated spin density on the acceptor as a function of time is shown in figure 3A.2.

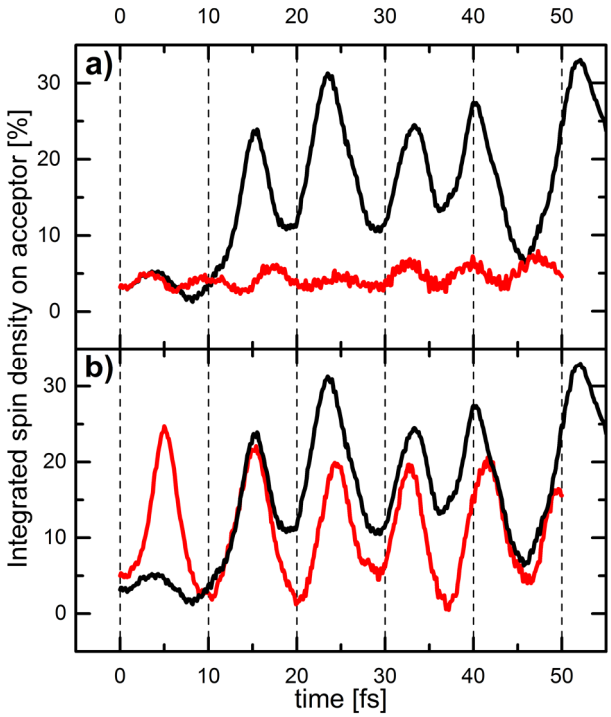

Figure 3A.2. Comparison of the electron transfer pattern for unconstrained nuclear degrees of freedom (black) with the transfer pattern of a simulation with the nuclear coordinates kept fixed at the initial geometry (simulation G0, **a**, red) and with the pattern for fixed nuclear coordinates at the geometry taken at 10.7 fs of the original trajectory, when the electron transfer starts (simulation G1, **b**, red).

A frequency analysis of the electron transfer patterns of these three simulations is presented in figure 3A.3 The peaks at around 4300 cm^{-1} and 5500 cm^{-1} corresponding to the trajectory with free nuclei show significant overlap with the frequencies of electron density oscillations in the case of the frozen initial geometry (simulation G0). This strongly suggests that the high frequency oscillations are due to the coupling between electronic states at a geometry close to the Franck-Condon point. The main peak at about 3500 cm^{-1} shows instead significant overlap with the electron

density oscillation frequency extracted from simulation G1, where the nuclei were fixed at a geometry in the strong coupling regime. This is also the peak that has a large overlap with the N-H bond vibrations. This shows that at this specific geometry, a resonance between electronic energy difference and nuclear vibration (the N-H stretches) has emerged.

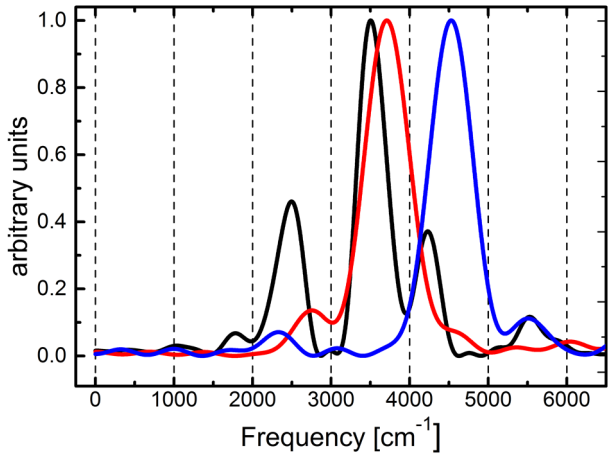

Figure 3A.3. Frequencies of electron transfer processes: in black, ET pattern during Ehrenfest simulation with free nuclear degrees of freedom, in blue ET transfer frequencies with nuclear degrees of freedom kept fixed at the initial geometry (simulation G0), in red ET transfer frequencies with nuclear degrees of freedom fixed for the geometry at the onset of electron transfer (approx. t = 10.7 fs, simulation G1).

3A.4 Assignment of relevant peaks in the total VDOS

The bond distances were extracted from the nuclear trajectory. FTs were performed on these bond distances to obtain the corresponding vibrational frequencies. By performing a FT on the velocity autocorrelation function, a total VDOS of the entire system was obtained. A gaussian window function with a sigma value of 0.8 was chosen to filter out noise in the FT. In order to assign specific peaks in the total VDOS, we analyze the time evolution of specific localized geometric parameters such as bond distances and angles extracted from the trajectory. FTs reveal the underlying frequencies. We find that the highest frequency band at $\nu \approx 3500$ cm^{-1} can clearly be associated with N-H stretching modes as shown in figure 3A.4. The N-H bond involved in the central N···H-N hydrogen bond shows instead a considerably lower frequency, giving rise to a red shifted peak in the total VDOS at $\nu \approx 2700$ cm^{-1}. This can be explained by the relatively strong hydrogen bond, with the hydrogen almost being shared between the two nitrogen atoms. As shown in figures 3A.5 and 3A.6, the peak centered around 1500 cm^{-1} consists of several contributions from C=O stretches, C-N stretches and some bending modes. The overlap between many modes close in frequency make a direct association for ν < 2000 cm^{-1} in general

complicated. What clearly emerges through this vibrational analysis is the separation in frequency of the N-H bonds compared to all other vibrational modes.

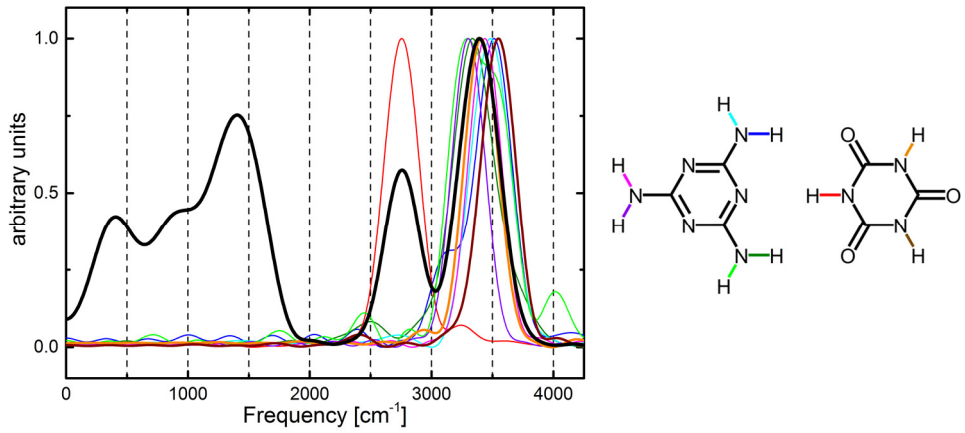

Figure 3A.4. VDOS of the pseudo base pair obtained via FT of the velocity autocorrelation function extracted from the Ehrenfest trajectory (black). Shown in color are all frequencies of the N-H stretches obtained via FT of the bond distances extracted from the Ehrenfest trajectory. The corresponding bonds are color-coded in the chemical structure shown on the right. Interesting is the shifted frequency of the central N-H bond on the donor-acceptor interface, as its frequency is significantly shifted to lower values due to the weakening of the bond through the strong hydrogen bond formed.

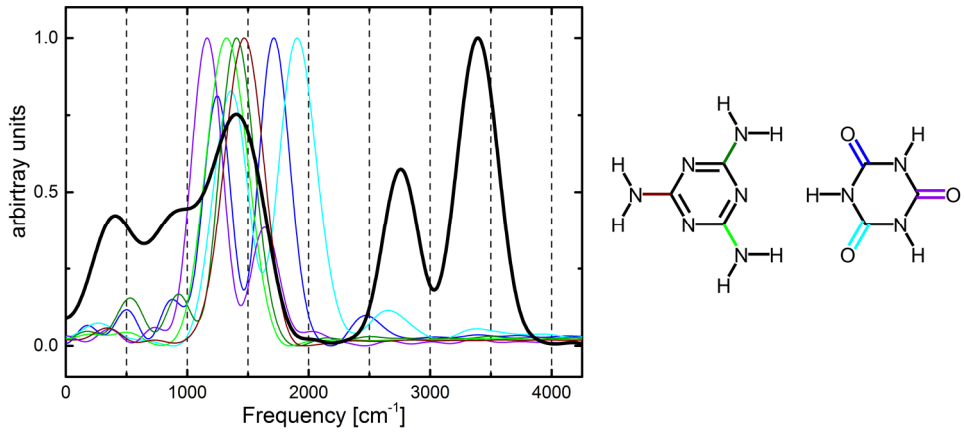

Figure 3A.5. VDOS of the pseudo base pair obtained via FT of the velocity autocorrelation function extracted from the Ehrenfest trajectory (black). Shown in color are frequencies of C=O stretches and C-N stretches obtained via FT of the bond distances extracted from the Ehrenfest trajectory. The corresponding bonds are color-coded in the chemical structure shown on the right.

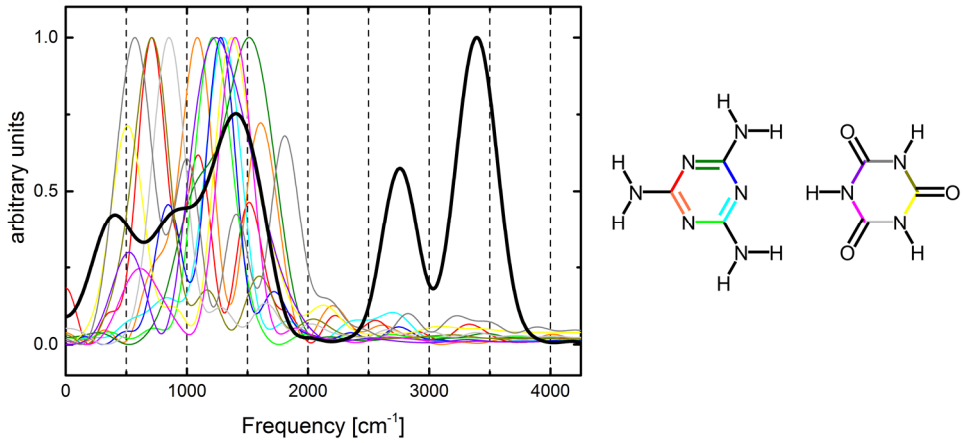

Figure 3A.6. VDOS of the pseudo base pair obtained via FT of the velocity autocorrelation function extracted from the Ehrenfest trajectory (black). Shown in color are frequencies of ring vibrations obtained via FT of the bond distances extracted from the Ehrenfest trajectory. The corresponding bonds are color-coded in the chemical structure shown on the right.

Figure 3A.7 shows the total VDOS for the two simulations using ^{1}H and ^{2}D respectively. The N-H (N-D) stretches are shifted as expected on the basis of the mass difference.

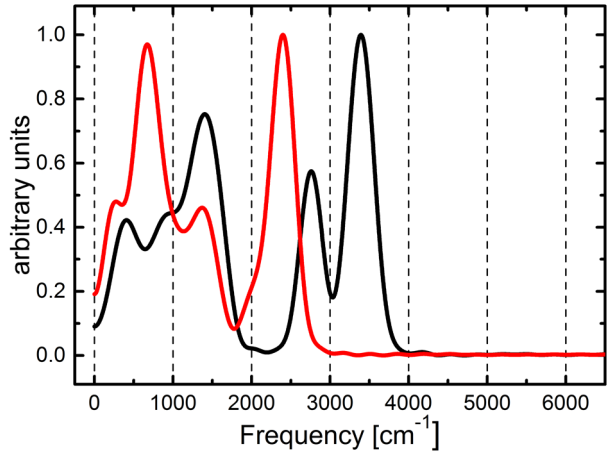

Figure 3A.7. Total VDOS of the ^{2}D substituted (red) and ^{1}H systems (black), obtained by performing a FT of the velocity autocorrelation functions using the respective trajectories.

3A.5 Dynamic Symmetry breaking

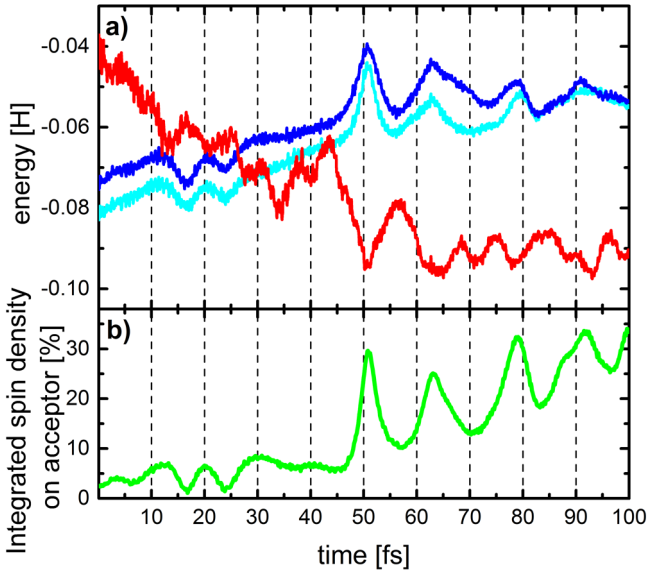

Figure 3A.8. Time evolution of the orbital energies (**a**) of the LUMO+2 (red), LUMO+1 (dark blue) and LUMO (light blue) in comparison to the electron transfer (green, **b**) during the Ehrenfest dynamics simulation starting with a C_{2v}-enforced initial geometry.

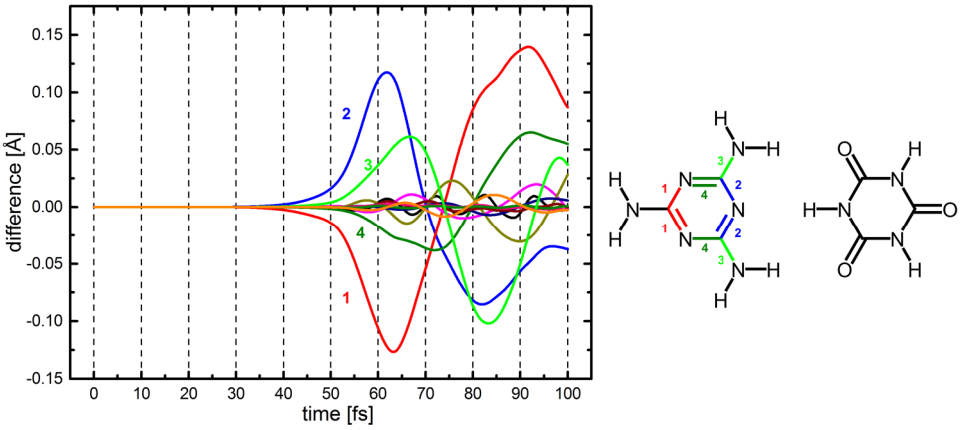

Figure 3A.9. Difference in bond distance between symmetry equivalent bond pairs. Here, the bond distance of the bonds shown as lower in the chemical structure is subtracted from the bond distance of their respective symmetry equivalent bond above. Color-coded are the four bond pairs first diverging from perfectly symmetric behavior.

3A.6 Dipole moment orientation

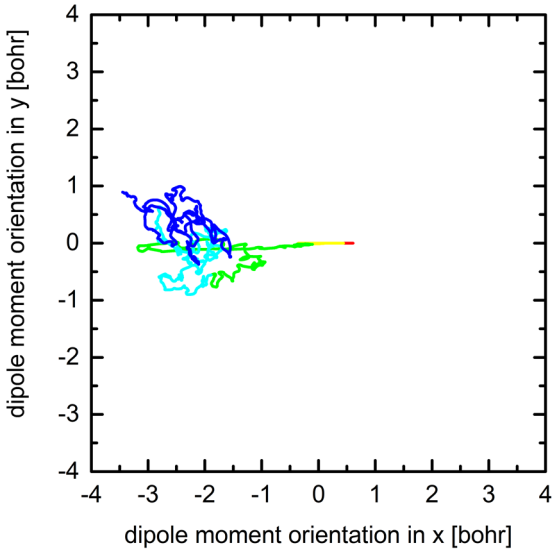

Figure 3A.10. Orientation of the dipole moment associated with β-electrons in the x-y plane for the simulation with enforced symmetric starting geometry. The colors correspond to consecutive time intervals, starting from red ($0<t<20$ fs) over yellow ($20<t<40$ fs), green ($40<t<60$ fs), light blue ($60<t<80$ fs) and dark blue ($80<t<100$ fs). A rotational character is visible in this case as well, but seems to be obscured by the large change in x due to the generated charge transfer state.

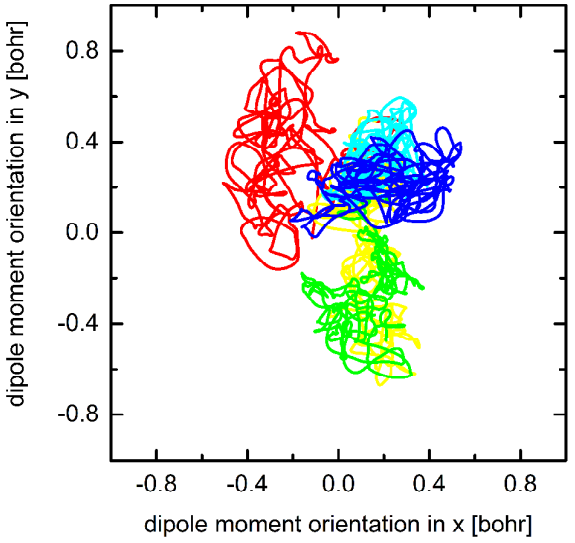

Figure 3A.11. Orientation of the dipole moment associated with α-electrons in the x-y plane for the simulation without enforced symmetry. The colors correspond to consecutive time intervals, starting from red ($0<t<20$ fs) over yellow ($20<t<40$ fs), green ($40<t<60$ fs), light blue ($60<t<80$ fs) and dark blue ($80<t<100$ fs). Rotational character, yet noisy, is apparent also in this simulation.

3A.7 Estimated non-adiabaticity of the process via the two level model by Purchase et al.[8]

Following the model discussed in chapter 2 and in Purchase *et al* [8], we consider the formula (see equation 2.31) for the period τ needed to convert the reactant state to the product state during the nonadiabatic process:

$$\tau = \frac{\pi}{R_0 d_{12} \omega_n}$$

We should keep in mind, that this result is obtained for a simple two state model that is coupled to a single nuclear vibrational mode of frequency ω_n with displacement R_0. Due to sweep of the resonance condition between the nuclear vibration and energy difference between the electronic states, the two state model gives a good description of the conversion process as the resonance leads to truncation of the full Hamiltonian, collapsing to two states.[8] To get a rough estimate of the nonadiabatic coupling term d_{12} for our donor-acceptor molecular complex, we therefore choose the most relevant nuclear mode which is coupled to the electronic motion. We consider the case with symmetric starting conditions (figure 3.1c), where the central N-H bond vibration is the most relevant mode, with $\omega_n \sim 2\pi*2700$ cm^{-1} (see figure 3A.4). The displacement R_0 of this mode is determined from the trajectory to be approximately 0.04 Å (see figure 3.2a). As a rough estimate for the complete charge transfer process, we take the time from the onset of electron transfer to the end of the simulation (55 fs, see figure 3.1c) and multiply by 3 to extrapolate to full electron transfer. In this way we estimate a period τ = 165 fs. By using these parameters extracted from our system, we estimate a value of 0.94 Å^{-1} for d_{12}.

3A.8 References

(1) Velde, G. te; Bickelhaupt, F. M.; Baerends, E. J.; Fonseca Guerra, C.; van Gisbergen, S. J. A.; Snijders, J. G.; Ziegler, T. Chemistry with ADF. *J. Comput. Chem.* **2001**, *22* (9), 931–967.

(2) ADF2013, http://www.scm.com, SCM, Theoretical Chemistry, Vrije Universiteit, Amsterdam, The Netherlands. .

(3) Becke, A. D. Density-Functional Exchange-Energy Approximation with Correct Asymptotic Behavior. *Phys. Rev. A* **1988**, *38* (6), 3098–3100.

(4) Lee, C.; Yang, W.; Parr, R. G. Development of the Colle-Salvetti Correlation-Energy Formula into a Functional of the Electron Density. *Phys. Rev. B* **1988**, *37* (2), 785–789.

(5) Yanai, T.; Tew, D. P.; Handy, N. C. A New Hybrid Exchange–Correlation Functional Using the Coulomb-Attenuating Method (CAM-B3LYP). *Chem. Phys. Lett.* **2004**, *393* (1–3), 51–57.

(6) Van Lenthe, E.; Baerends, E. J. Optimized Slater-Type Basis Sets for the Elements 1–118. *Journal of Computational Chemistry* **2003**, *24*, 1142–1156.

(7) Grimme; others. A Consistent and Accurate Ab Initio Parametrization of Density Functional Dispersion Correction (DFT-D) for the 94 Elements H-Pu. *J. Chem. Phys.* **2010**, *132* (715).

(8) Purchase, R. L.; de Groot, H. J. M. Biosolar Cells: Global Artificial Photosynthesis Needs Responsive Matrices with Quantum Coherent Kinetic Control for High Yield. *Interface focus* **2015**, *5* (3), 20150014.